Applied Catalysis B: Environmental 336 (2023) 122951

Contents lists available at ScienceDirect

Applied Catalysis B: Environmental

journal homepage: www.elsevier.com/locate/apcatb

High-loading of well dispersed single-atom catalysts derived from Fe-rich marine algae for boosting Fenton-like reaction: Role identification of iron center and catalytic mechanisms

Kexin Yin [a,1], Lijing Peng [a,1], DongDong Chen [a], Siyi Liu [a], Yujie Zhang [a], Baoyu Gao [a], Kaifang Fu [c], Yanan Shang [a,b,*], Xing Xu [a,**]

[a] Shandong Key Laboratory of Water Pollution Control and Resource Reuse, School of Environmental Science and Engineering, Shandong University, Qingdao 266237, PR China
[b] College of Safety and Environmental Engineering, Shandong University of Science and Technology, Qingdao 266590, PR China
[c] School of Civil and Environmental Engineering, Shandong Jianzhu University, Jinan 250101, PR China

ARTICLE INFO

Keywords:
High iron-loading
Single-atom catalysts (SACs)
Iron
Marine algae
Fenton-like reaction

ABSTRACT

Developing single-atom catalysts (SACs) with superior Fenton-like performance and low-cost via green synthesis strategy is an urgent problem. It was for the first time to prepare the iron single-atom catalyst (Fe-SAC) with highly atomically-dispersion from natural Fe-rich marine algae (*Enteromorpha*) with iron amount over 1.5 wt%. Iron screening test indicated that the activation performance of *Enteromorpha*-derived Fe-SACs catalyst was mainly based on Fe-N_4-C sites, and the roles of radicals accompanying with Fe(IV) and $^1O_2$ oxidation showed very small contributions. In contrast, the degradation of organic was dominated by the electron-transfer process (ETP), and the ETP mechanism was greatly enhanced by the iron centers in the *Enteromorpha*-derived Fe-SACs, which could help extract more electrons from the organics to the Fe-N_4-C/PMS complex, thus facilitating the ETP in catalytic system. In addition, the commercial ceramic membrane (CM) coated with *Enteromorpha*-derived Fe-SACs catalyst showed superior catalytic activtiy with a stable water flux.

1. Introduction

Advanced oxidation processes (AOPs) generate strong oxidizing free radicals by activating oxidants, which can completely mineralize or decompose most refractory organic pollutants in water bodies, and show broad application prospects [1–6]. The peroxymonosulfate (PMS) oxidation technology based on sulfate radical ($SO_4^{\bullet-}$) is a new advanced oxidation technology [5,7–11]. At present, the construction of new efficient heterogeneous catalytic system is the main research direction of PMS oxidation technology, the core of which is to design high-performance and low-cost heterogeneous catalysts to activate PMS to generate reactive oxygen species (ROS) and achieve efficient degradation of pollutants [10–17].

Due to the unique electronic and coordination structure and excellent performance in advanced oxidation, single atom catalysts (SACs) have become the frontier and hotspot in the field of AOPs [5,12,18,19]. At present, a variety of synthesis strategies (pyrolysis, wet chemical synthesis, physical and chemical vapor deposition, electrochemical deposition, ball milling, etc.) have been used to prepare versatile SACs [20–24]. However, these methods are often complicated, costly and low yield, which are not conducive to the large-scale preparation of SACs for AOPs [25–27]. Researchers have found that the pyrolysis strategy using carbon and nitrogen-rich materials (nitrogen-containing organic macromolecules or compounds, MOF and its derivatives, biomass, etc.) as precursors has great application and development prospects in the large-scale preparation of SACs [24–28]. Compared with other nitrogen-doped carbon materials, nitrogen-containing biomass materials are very favorable for large-scale synthesis of SACs as carbon carriers due to their low cost and abundant resources [19,29–32]. However, a large number of costly metal precursors should be added into the

* Corresponding author at: Shandong Key Laboratory of Water Pollution Control and Resource Reuse, School of Environmental Science and Engineering, Shandong University, Qingdao 266237, PR China.
** Corresponding author.
E-mail addresses: shangyanan@sdust.edu.cn (Y. Shang), xuxing@sdu.edu.cn (X. Xu).
[1] Kexin Yin and Lijing Peng are co-first authors.

https://doi.org/10.1016/j.apcatb.2023.122951
Received 2 March 2023; Received in revised form 21 April 2023; Accepted 31 May 2023
Available online 2 June 2023
0926-3373/© 2023 Elsevier B.V. All rights reserved.

pyrolysis system and react with the nitrogen-containing biomass materials to form the single atom sites via complicated routines, and most of the costly metal precursors would be inevitably lost during the pyrolysis and subsequent washing procedures [30,32,33]. Therefore, it is still an urgent problem to prepare SACs with stable performance and low cost by green synthesis process.

As a transition metal, iron exists in many biomass materials in nature [31,32,34]. Recently, a series of SACs have been prepared by using the Fe-rich biomasses as precursors [31,32,34]. However, the Fe amounts in most of these biomasses are very low [31,32]. For example, spirulina and auricularia auricular-judae have been used as the iron-based precursors for SACs preparation, but their iron contents are below 0.1 wt%, which make the SACs derived Fe-rich biomasses with very limit metal single-atom sites for Fenton-like reactions [31,32]. The exceptional thing is that the iron content of Marine algae (*Enteromorpha*) is up to 0.2–0.5 wt%, which is much higher than that of other Marine algae and biomass materials [34]. However, direct pyrolysis of *Enteromorpha* would inevitably result in the aggregation of Fe species to form Fe nanoclusters due to the lack of coordination elements such as nitrogen for anchoring iron [34]. Intriguingly, in addition to its iron-rich property, *Enteromorpha* contains a large number of capillary structures, which exhibits super-strong water adsorption ability. Therefore, the adsorption of nitrogen-containing small molecules from nitrogen-rich solutions (such as urea solution) by *Enteromorpha* powder can effectively improve the nitrogen content in *Enteromorpha*, which is beneficial to coordinate and assist anchoring more iron elements during high-temperature pyrolysis and avoid the formation of Fe-Fe bonds. Thus, the atomic-level dispersion of iron in *Enteromorpha* onto the carbon matrixes can be realized and the *Enteromorpha*-derived Fe single-atom (Fe-SACs) catalysts with active Fe-N_x centers can be large-scale prepared.

In this work, the distribution of nitrogen content in *Enteromorpha* can be promoted by increasing the absorption content of urea onto *Enteromorpha*, and the *Enteromorpha*-derived SACs with atomically dispersed Fe-N_x coordination structures were prepared by in-situ coordination with the iron element in *Enteromorpha* during high-temperature pyrolysis. The low-cost *Enteromorpha*-derived SACs were also immobilized onto the commercial ceramic membrane (CM) for continuous operation in Fenton-like system. The role of iron single-atom derived from the intrinsic iron species in *Enteromorpha* on the catalytic activity, as well as catalytic pathway were identified via iron screening test, open-circuit potential, in situ Raman and salt bridge analysis. We think this study exhibits an interesting strategy for large-scale preparation of low-cost SACs for Fenton-like systems, and also provides the new understanding on the catalytic activity and catalytic pathway triggered by the iron single-atom derived from Fe-rich biomass.

2. Materials and methods

2.1. Chemicals

The *Enteromorpha* in this study was obtained from Qingdao Jimo coastal port located on the east coast of China (36◦05 'N, 120◦18' E). The chemical materials, including ethanol (EtOH), peroxymonosulfate (PMS), tert-butyl alcohol (TBA), 5,5 −dimethylpyrroline–oxide (DMPO), urea, furfuryl alcohol (FFA), methyl phenyl sulfoxide (PMSO), H_2SO_4 (98%), Na_2SO_4, polyvinyl alcohol (PVA), succinic acid, nafion, KCl, were obtained from Sinopharm Chemical Reagent Co. Ltd. Various pollutants, including bisphenol A (BPA), naproxen (NPX), carbamazepine (CBZ), sulfanilamide (SA), were purchased from Aladdin Co. Ltd., China. The commercial ceramic membrane (CM) was obtained from Suzhou Environmental Technology Co. Ltd. The glassy carbon electrode (GCE) was obtained from Shanghai Jinzhan Industrial Technology Co., LTD.

2.2. Fabrication of Enteromorpha-derived Fe-SACs catalysts

The *Enteromorpha* powder was mixed with 50 mL of urea solution (2.5 M or 5.0 M), and then stirred at room temperature for 10 h. The mixture was lyophilized at − 60 °C, ground to powder, and then placed in a quartz vessel. The powder was pyrolysis at 900 °C for 2 h under the atmosphere of nitrogen at a heating rate of 10 °C/min. The obtained primary products were stirred and soaked in 0.5 M H_2SO_4 solution for 12 h to remove unstable metal substances. The resulting powder was washed with deionized water to neutral, dried and stored for use.

2.3. Fabrication of Fe-SACs/CM via spray-crosslinking method

For applying the *Enteromorpha*-derived Fe-SACs in a continuous Fenton-like system, a novel strategy of spray-crosslinking was developed for integrating the as-prepared Fe-SACs onto the surface of commercial CM. Spraying step could rapidly deposit the Fe-SACs on the large membrane surface, and the crosslinking step could firmly immobilize the Fe-SACs on the CM without vacuum installations or complex high pressure. As a result, this strategy could be easily applied for fabricating a larger Fenton-like catalytic membrane. First, 1.0 g of Fe-SACs prepared from of urea (2.5 M)-saturated *Enteromorpha* was added into 60 mL PVA solution (5 mg/mL) and ultrasonically dispersed for 20 min. Thereafter, the *Enteromorpha*-derived Fe-SACs ink was evenly sprayed on the surface of CM (10 cm × 25 cm) with an airbrush (Hansa Infinity, Germany). The same operation was also repeated for coating the *Enteromorpha*-derived Fe-SACs on the other side of the membrane. The coated CM was immersed into 1.0 wt% of succinic acid solution for 2 h and then dried at 60 °C for 6–8 h. The resulting catalytic membrane was heated at 250 °C in air to remove residual agents and named as Fe-SACs/CM.

2.4. Experimental procedure

The degradation of NPX was conducted by adding 5 mg of *Enteromorpha*-derived Fe-SACs catalyst with PMS (1.0 mM) into 50 mL of NPX solutions. The solution (1 mL) was collected at required time interval and filtered via a 0.22 μm film. The filtrate was mixed with 0.5 mL sodium thiosulfate to quench the radicals, and then the residual NPX was detected by a high-performance liquid chromatograph (HPLC, UltiMate 3000) with a C-18 column. All degradation tests were carried out at pH 6.0. In addition, the reactive oxygen species (ROS) in the *Enteromorpha*-derived Fe-SACs/PMS system were determined by adding the scavengers (e.g., TBA (200 mM), and EtOH (200 mM), PMSO (5 mM)) into the catalytic systems. D_2O as solution was employed to replace the H_2O for determining the role of singlet oxygen ($^1O_2$). Different concentrations (1, 5, and 10 mM) of phenanthroline were added into the *Enteromorpha*-derived Fe-SACs/PMS system as iron screening agent to determine the role of iron single-atom in *Enteromorpha*-derived Fe-SACs. Degradation performances of *Enteromorpha*-derived Fe-SACs for other organics via PMS activation have also been conducted. The catalytic tests of Fe-SACs/CM towards NPX were conducted using a flow through setup driven via a diaphragm pump.

2.5. Characterization and analysis methods

The properties (e.g., coordination structures, microstructures, metal content) of the *Enteromorpha*-derived Fe-SACs catalysts were determined by various measurements, which were given in Appendix S1. Other experimental procedures, including electrochemical measurements (open circuit potential, and galvanic oxidation system (GOS)), electron paramagnetic resonance (EPR), DFT calculation were given in Appendix S2-S6.

3. Results and discussions

3.1. Coordination structures of Enteromorpha-derived Fe-SACs

The *Enteromorpha*-derived Fe-SACs with well iron-atom dispersion were prepared by saturating the *Enteromorpha* with 2.5 M or 5.0 M of urea solution (Fig. 1a). The nitrogen-rich urea in the urea solutions could be saturated onto the dried *Enteromorpha* powder and flowing throughout the skeleton of *Enteromorpha* via the capillaries. This process can effectively increase the nitrogen content of *Enteromorpha*, and the nitrogen (32.13 wt%) in urea-saturated *Enteromorpha* (before pyrolysis) was several orders of magnitude higher than the intrinsic iron (<0.5 wt %), which can be efficiently dispersed into the capillaries of *Enteromorpha* to better contact with the intrinsic iron in *Enteromorpha*. TEM mappings of the urea-saturated *Enteromorpha* (before pyrolysis) were given in Fig. S1, which showed the highly dispersed nitrogen species in the capillaries of *Enteromorpha*. As a result, the high nitrogen in urea-saturated *Enteromorpha* is beneficial to coordinate more iron elements via the assistance of capillaries of *Enteromorpha* during high-temperature pyrolysis, so as to maximize the avoid of Fe-Fe bond formation.

The X-ray absorption fine structure (XAFS) can provide the coordination information on the *Enteromorpha*-based SACs. The data of X-ray absorption near-edge structure (XANES) can evaluate the valence state of Fe, while extended X-ray absorption fine structure (EXAFS) can obtain the local coordination environment of Fe. As shown in Fig. 1b and Table S1, the EXAFS analysis showed that the coordination structure of *Enteromorpha*-derived Fe-SAC prepared from 2.5 M or 5.0 M of urea saturated *Enteromorpha* was based on Fe-N_4-C configuration (coordination number of 3.60 for 2.5 M of urea saturated *Enteromorpha*, and 4.35 for 5.0 M of urea saturated *Enteromorpha*). In contrast, Fe-SACs prepared via the direct pyrolysis of urea-free *Enteromorpha* exhibited the existence of Fe-N_2O_2 coordination, accompanying with large amounts of Fe-Fe bonds (Fig. S2). This result indicated that the iron clusters accounted for a large fraction of the iron species in the Fe-SACs prepared from urea-free *Enteromorpha*. The Fe K-edge XANES spectra of *Enteromorpha*-derived Fe-SACs catalysts indicated that the Fe state was located between Fe^{2+} and Fe^{3+} (Fig. 1c and Fig. S3) [35]. Wavelet transform (WT) contour plots of Fe-SACs prepared from urea-free *Enteromorpha* showed the intensity maximum at ~4.5 Å, which was assigned to the Fe-N(O)

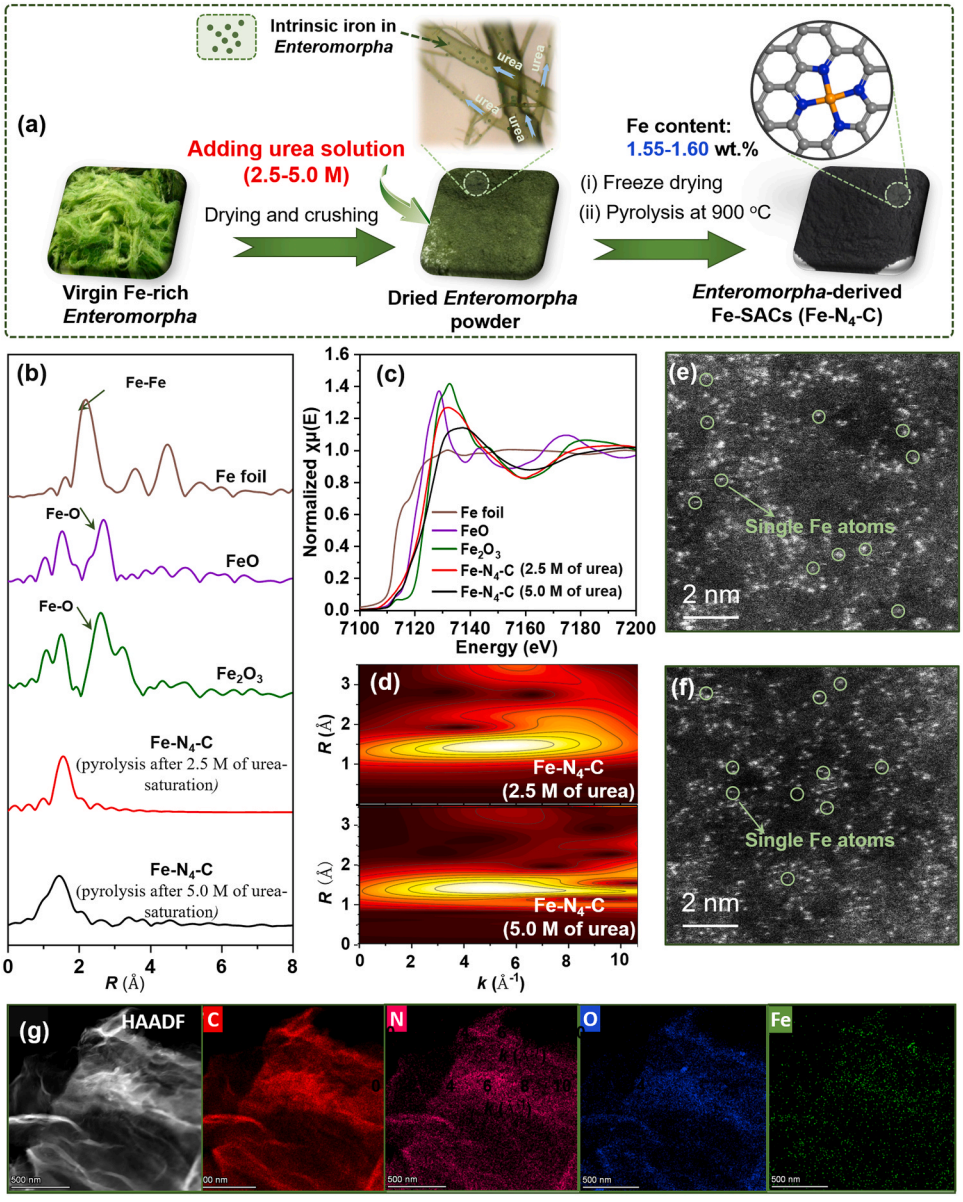

Fig. 1. (a) Fabricating scheme of Fe-SACs from Fe-rich *Enteromorpha* after urea saturation (No additional iron salts); (b) FT-EXAFS spectra for Fe K-edge of *Enteromorpha*-derived Fe-SACs prepared from 2.5 M and 5.0 M of urea-saturated *Enteromorpha*; (c) Fe K-edge XANES spectrum of *Enteromorpha*-derived Fe-SACs with coordination structure of Fe-N_4-C (2.5 M and 5.0 M of urea-saturated *Enteromorpha*); (d) WT contour plots of *Enteromorpha*-derived Fe-SACs prepared from urea-saturated *Enteromorpha* (Fe-N_4-C); (e) HAADF-STEM of Fe-N_4-C (2.5 M of urea-saturated *Enteromorpha*); (f) HAADF-STEM of Fe-N_4-C (5.0 M of urea-saturated *Enteromorpha*); and (g) The EDX mappings of Fe-N_4-C (2.5 M of urea-saturated *Enteromorpha*).

coordination (Fig. 1d and Fig. S4). However, a plot at ~9.2 Å was observed corresponding to the formation of Fe atomic clusters due to the aggregation of iron species in urea-free *Enteromorpha* after direct pyrolysis. In contrast, the plot at ~9.2 Å was disappeared in the Fe-N_4-C prepared from urea-saturated *Enteromorpha*, indicating that the Fe-Fe bonds in the *Enteromorpha*-derived Fe-SACs was significantly reduced via the coordination of Fe species with nitrogen in urea.

The HAADF-STEM image of Fe-SACs prepared after the direct pyrolysis of urea-free *Enteromorpha* showed that the carbon matrixes were fixed with large amounts of Fe clusters with scattered Fe single-atom (Fig. S5). As a result, the atomically dispersed Fe-N_2O_2 structure (well dispersed dots) accounted for a very small fraction of Fe species. In contrast, *Enteromorpha* saturated with 2.5 M or 5.0 M of urea provided a large number of nitrogen course for iron coordination, and no obvious Fe clusters can be observed. These results indicated that the Fe clusters prepared from urea-free *Enteromorpha* were almost transferred into the Fe single-atom (Fig. 1e and f), which confirmed the well coordination of Fe in urea-saturated *Enteromorpha*. In addition, the dispersion of atom iron sites seemed to be further improved with the increasing urea concentration from 2.5 M to 5.0 M. As a result, the addition of more urea could provide more nitrogen source for coordinating the iron species to form the atom iron sites. The EDX mappings of *Enteromorpha*-derived Fe-SACs with coordination structure of Fe-N_4-C also showed the well dispersed Fe species in the *Enteromorpha*-based carbon matrixes (Fig. 1g).

The N contents (wt%) of Fe-N_4-C (2.5 M and 5.0 M of urea-saturated *Enteromorpha*) were significantly increased to 5.53–6.97 wt% as compared with that (1.44 wt%) of Fe-N_2O_2 (Fig. S6); this was similar to the N fractions of the Fe-N_2O_2 (1.26 at%) and Fe-N_4-C (4.54–5.63 at%) determined from the XPS N1s spectra (Table S2, Fig. 2a and b). The XPS N 1 s spectra of Fe-N_4-C prepared from urea-saturated *Enteromorpha* showed increasing pyridinic N fraction (38.0–39.2%) as compared with that (31.4%) of Fe-SACs prepared from urea-free *Enteromorpha* (Fig. 2a, b and Table S2). Since the N contents (wt%) of Fe-N_4-C were 4–5 times higher than that of Fe-N_2O_2, the amounts of pyridinic N species in Fe-N_4-C were almost more than 4 times higher than in Fe-N_2O_2 to coordinate the iron single-atoms in Fe-N_4-C. In addition, the iron content in the Fe-SACs prepared from urea-free *Enteromorpha* was approximately 0.84 wt %. It was then increased to 1.55 wt% in Fe-N_4-C (2.5 M of urea-saturated *Enteromorpha*) and further slightly increased to 1.60 wt% in Fe-N_4-C (5.0 M of urea-saturated *Enteromorpha*) as shown in Table S3. As a result, the addition of N contents due to the urea saturation in iron-rich *Enteromorpha* could immobilize more iron element from iron-rich *Enteromorpha* to achieve (i) more uniformly dispersed Fe single-atom in the carbon matrixes, and (ii) higher coordination numbers from Fe-N_2O_2 to Fe-N_4-C in the *Enteromorpha*-derived Fe-SACs.

XRD patterns of Fe-N_4-C (2.5 M and 5.0 M of urea-saturated *Enteromorpha*) and Fe-N_2O_2 were given in Fig. 2c. The strong crystal peaks in the Fe-N_2O_2 were ascribed to the minerals in the *Enteromorpha* ($CaSO_4$ crystals, with XRD card number: PDF#70–0982). After urea-saturation, the intensity of these crystal peaks was greatly reduced (Fig. 2c), which might due to that (i) the carbon fractions in the urea-saturated catalysts were greatly augmented by using the urea as carbon and nitrogen sources, and (ii) most $CaSO_4$ crystals could not be captured by the urea and they were excreted from the capillaries of *Enteromorpha* by the urea solution. Raman spectra also showed certain change in the carbon skeleton of Fe-N_4-C (2.5 M and 5.0 M of urea-saturated *Enteromorpha*) and Fe-N_2O_2 (urea-free *Enteromorpha*). The I_D/I_G of Fe-N_2O_2 was located at 0.995 (Fig. 2d). In contrast, the ratios of I_D/I_G were increased to 1.104–1.108 for Fe-N_4-C (2.5 M and 5.0 M of urea-saturated *Enteromorpha*). This implied that more defective edges were generated in the carbon skeleton of Fe-N_4-C via the pyrolysis treatment of urea-saturated *Enteromorpha*.

3.2. Catalytic performance and the identification of the roles of reactive species

Two kinds of Fe-SACs derived from Fe-rich *Enteromorpha* by urea-

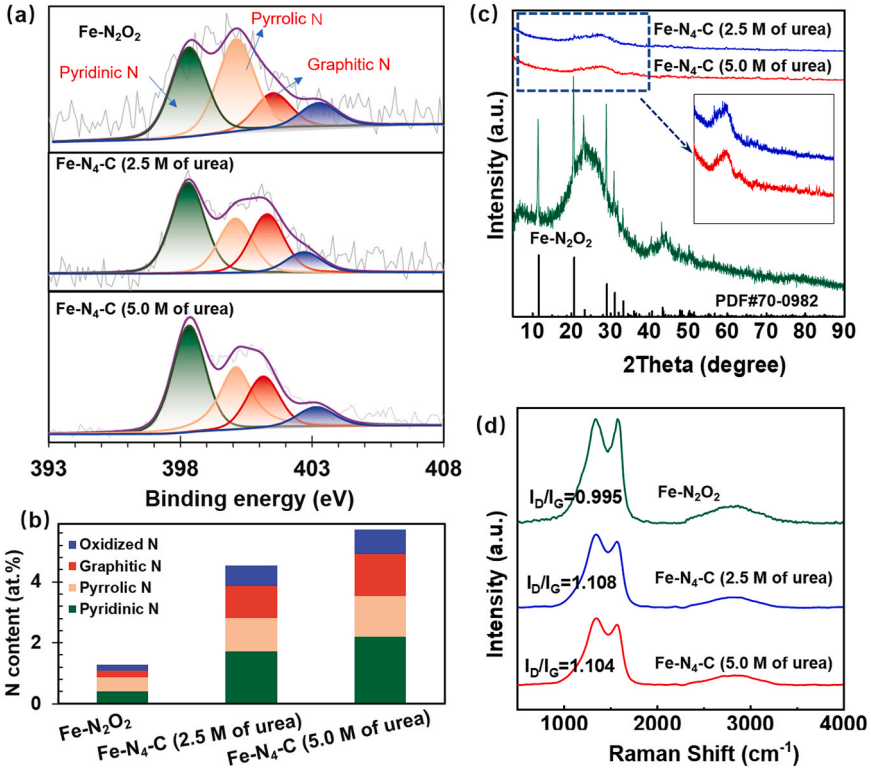

Fig. 2. (a) XPS N1s of Fe-N_2O_2 (urea-free *Enteromorpha*) and Fe-N_4-C (2.5 M and 5.0 M of urea-saturated *Enteromorpha*); (b) N contents (at%) of different catalysts as well as the fractions of different N species; (c) XRD patterns of different catalysts; (d) Raman spectra of different catalysts.

saturation or urea-free showed versatile degradation activity towards the NPX via PMS activation. The Fe-SACs (Fe-N_2O_2) prepared via the direct pyrolysis of urea-free *Enteromorpha* showed more than 96% of NPX degradation within 30 min with the degradation rate (k_{obs}) of 0.120 min^{-1} (Fig. 3a and b). In contrast, the k_{obs} values of Fe-N_4-C (2.5 M and 5.0 M of urea-saturated *Enteromorpha*) was substantially increased to 0.407–0.416 min^{-1} as compared with that of urea-free *Enteromorpha*. As shown in Fig. S7 and Table S4, the Fe-N_2O_2 exhibited inferior catalytic performance although the surface area and pore volume of Fe-N_2O_2 were almost three times higher than those of Fe-N_4-C (2.5 M of urea-saturated *Enteromorpha*). This result indicated that the reactivity of the catalysts was not based on the surface characteristics. As a result, the improvement of Fe-N_4-C compared to Fe-N_2O_2 could be ascribed to the increase of iron content. Considering the existence of high $CaSO_4$ content in the Fe-N_2O_2, the $CaSO_4$ with the same dosage (0.1 g/L) was mixed with PMS for NPX degradation. Results showed that the NPX cannot be degraded by adding the $CaSO_4$ (Fig. S8). As a result, the content of $CaSO_4$ did not affect the reactivity.

To further distinguish the effect of Fe–N_4 sites and N-doped carbon in the *Enteromorpha*-derived Fe-SACs catalyst (2.5 M of urea-saturated *Enteromorpha*), the iron screening experiments were conducted by using phenanthroline to poison the nonplanar Fe–N_4 sites, because phenanthroline can form a stable chelate complex with iron cations at pH= 2.0–9.0 so as to effectively poison the iron-centred catalytic sites in Fe-N_4-C [19,36]. As shown in Fig. 3a and b, when 1 mM of phenanthroline was added to the Fe-N_4-C/PMS system, the degradation of NPX still reached 97.8% with k_{obs} decreased from 0.407 min^{-1} to 0.0174 min^{-1}. The degradation of NPX was rapidly decreased to 23.4% by adding 5 mM of phenanthroline, and it was further decreased to 15.1% upon introducing 10 mM of phenanthroline. Similar result was also observed in the Fe-N_2O_2/PMS system, which showed that the degradation of NPX could be greatly decreased to 12.2% with the background of 10 mM of phenanthroline (Fig. S9). To further confirm the iron screening role of phenanthroline on the Fe–N_4 sites, a real space function named interaction region indicator (IRI) was employed to reveal chemical bonding and interaction between the phenanthroline and Fe–N_4 [37]. Vibration analysis results showed that a dipole derivative unit vector existed in the direction perpendicular to the Fe-N_4-C configuration, which suggested that Fe atom could vibrate on this configuration (Fig. S10). Results showed that the phenanthroline could

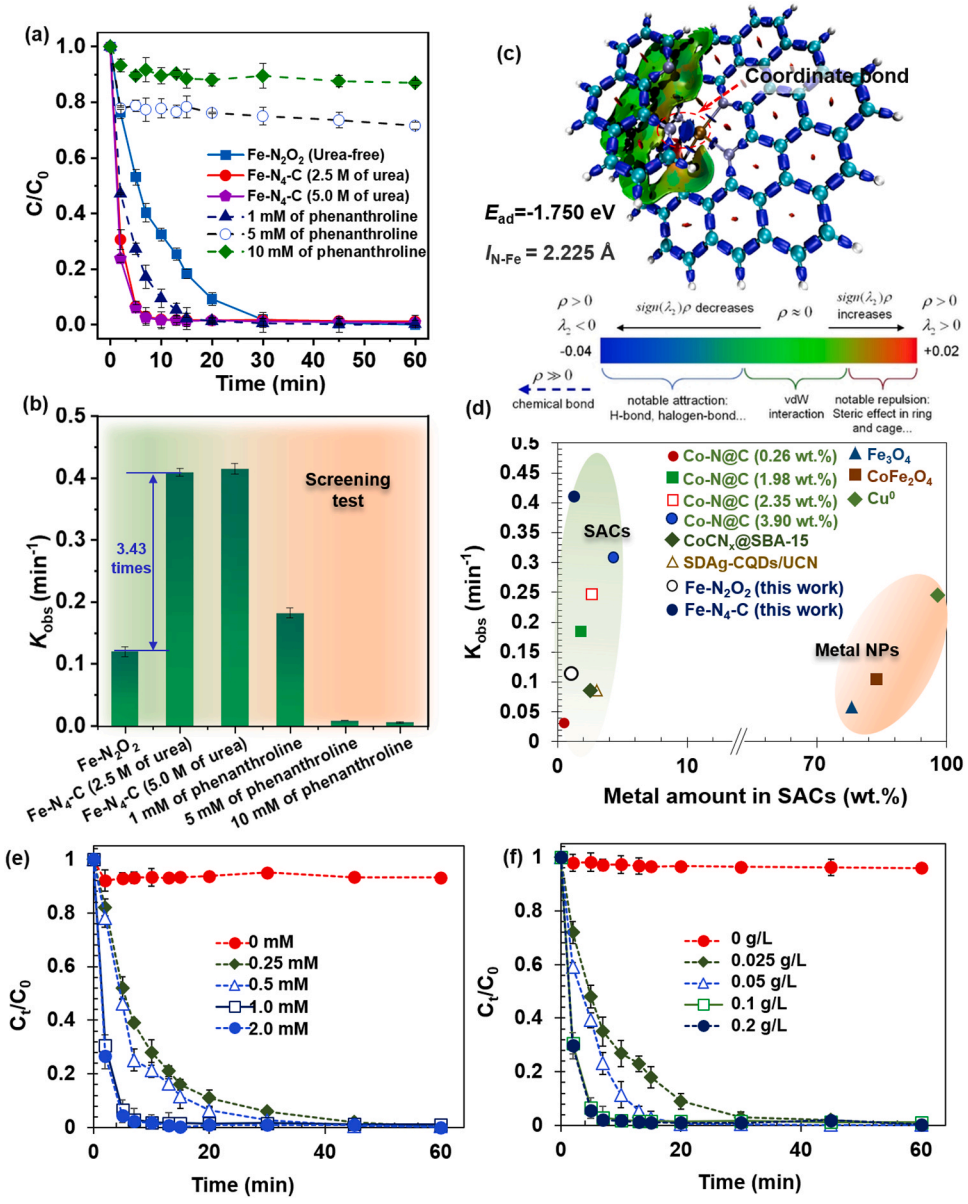

Fig. 3. (a) Catalytic performances of Fe-SACs derived from Fe-rich *Enteromorpha* as well the iron screening tests using phenanthroline to poison the Fe–N_4-C sites; (b) Their corresponding k_{obs} values; (c) The IRI isosurface map of phenanthroline coordinating with Fe-N_4-C (IRI = 1.0. The color scale represents standard coloring method and chemical explanation of sign(λ_2)ρ on IRI isosurfaces); (d) Comparison of metal amounts and catalytic activities in different metal catalysts; Catalytic activity of Fe–N_4-C at different (e) PMS dosages and (f) catalyst dosages (NPX: 10 mg/L; PMS: 1.0 mM; catalytic dosage: 0.1 g/L).

form a strong bonding with the nonplanar Fe–N_4 with binding energy (E_{ad}) of − 1.750 eV (Fig. 3c). The bond length of N-Fe ($l_{N\text{-}Fe}$) between phenanthroline and Fe–N_4 was calculated to be 2.225 Å. As a result, the strong binding of phenanthroline with Fe–N_4 led to irreversible loss of catalytic sites, which cannot provide enough sites to adsorb and activate PMS. Basically, the iron screening result indicates that the activation performance of the *Enteromorpha*-derived Fe-SACs catalyst was mainly due to the presence of Fe–N_4 sites, and the contribution of iron-free sites accounted for a minor role in the PMS activation.

The Fe-N_4-C catalysts used in subsequent tests was based the samples derived from 2.5 M of urea-saturated *Enteromorpha*. Effect of different pH conditions on the NPX oxidation in Fe-N_4-C/PMS system were given in Fig. S11. The pH in 3.0–6.0 showed very limited effect on NPX removal with almost constant k_{obs}, and the k_{obs} was decreased at pH of 9.0. This might be due to that the charge-transport process was inhibited under alkaline conditions via the electrostatic repulsion of SO_5^{2-} and catalytic sites, resulting in the inhibition of adsorption, and decomposition of PMS. The as-prepared Fe-SACs catalyst also exhibited strong anti-interference capacity in natural water, topwater and seawater, which indicated the promising prospective of *Enteromorpha*-derived Fe-SACs catalyst for actual environmental applications (Fig. S12 and S13). The *Enteromorpha*-derived Fe-SACs also showed extraordinary catalytic performance as compared with most reported metal loading catalysts for the oxidation processes (Fig. 3d, Fig. S14 and Table S5) [38–41]. The adsorption capacity of *Enteromorpha*-derived Fe-SACs catalyst (e.g., Fe-N_4-C) was negligible and the catalytic activity can be greatly increased with the increasing PMS dosage and catalyst dosage (Fig. 3e and f). After several cycles of degradation reaction, the catalytic stability of Fe-N_4-C still exceed 95% without the aggregation of iron centers as shown in the HAADF-STEM image of Fe-N_4-C after NPX degradation (Fig. S15 and S16), which indicated the stability of the intrinsic iron centers in Fe-N_4-C. The iron leaching was also detected, and the iron leaching was below 5 μg/L (Fig. S17). In addition, the fractions of N species in used Fe-N_4-C almost kept constant as compared with the original sample (Fig. S18). This result further confirmed the stability of Fe-N_4-C during catalytic reaction. The material cost for wastewater treatment was calculated as shown in Table S6. Considering the reusability of Enteromorpha-derived Fe-SACs, the actual cost would be lower.

The generated reactive species and associated catalytic mechanisms of *Enteromorpha*-derived Fe-SACs with well-dispersed Fe-N_4-C structures (derived from 2.5 M of urea-saturated *Enteromorpha*) were conducted via a series of quenching experiment and EPR spectra. EtOH is a typical probe with highly reactivity towards both $SO_4^{\bullet-}$ and $HO^{\bullet}$, and TBA is a selective scavenger for $HO^{\bullet}$ with $k_{HO\bullet,TBA}$ of 7.6×10^8 $M^{-1}S^{-1}$) [42,43]. In the Fe-N_4-C/PMS system, both $SO_4^{\bullet-}$ and $HO^{\bullet}$ showed very small contributions to the NPX degradation in the Fe-N_4-C/PMS system since the k_{obs} was only decreased by 2–5% by the addition of EtOH and TBA (Fig. 4a and Fig. S19). The $O_2^{\bullet-}$ radical was also analyzed via quenching test, which showed that there was no contribution of $O_2^{\bullet-}$ radical to the NPX oxidation (Fig. S20). The Fe(IV) species were always determined by using the PMSO probe. However, the PMSO could react with PMS which resulted in the reduction in the k_{obs} (Fig. 4a). As a result, the $PMSO_2$ generation in the *Enteromorpha*-derived Fe-SACs (Fe-N_4-C)/PMS systems were detected, which was only slightly increased as compared with that in PMS alone system (Fig. S21). This result indicated the weak Fe(IV) oxidation in the Fe-N_4-C/PMS systems (Fig. 4b). The existence of Fe(IV) oxidation in the Fe-N_4-C/PMS systems can be further confirmed by the oxidation of trans-stilbene toward trans-stilbene oxide (Fig. 4c), which showed a decrease in trans-stilbene and the generation of trans-stilbene oxide after the reaction [1]. Electron and hole quenching experiments also showed that there were no electron and hole roles in the system (Fig. S22). The EPR signals of $SO_4^{\bullet-}$ and $HO^{\bullet}$ were very weak in Fe-N_4-C/PMS system (Fig. S23). In contrast, the EPR spectra exhibited

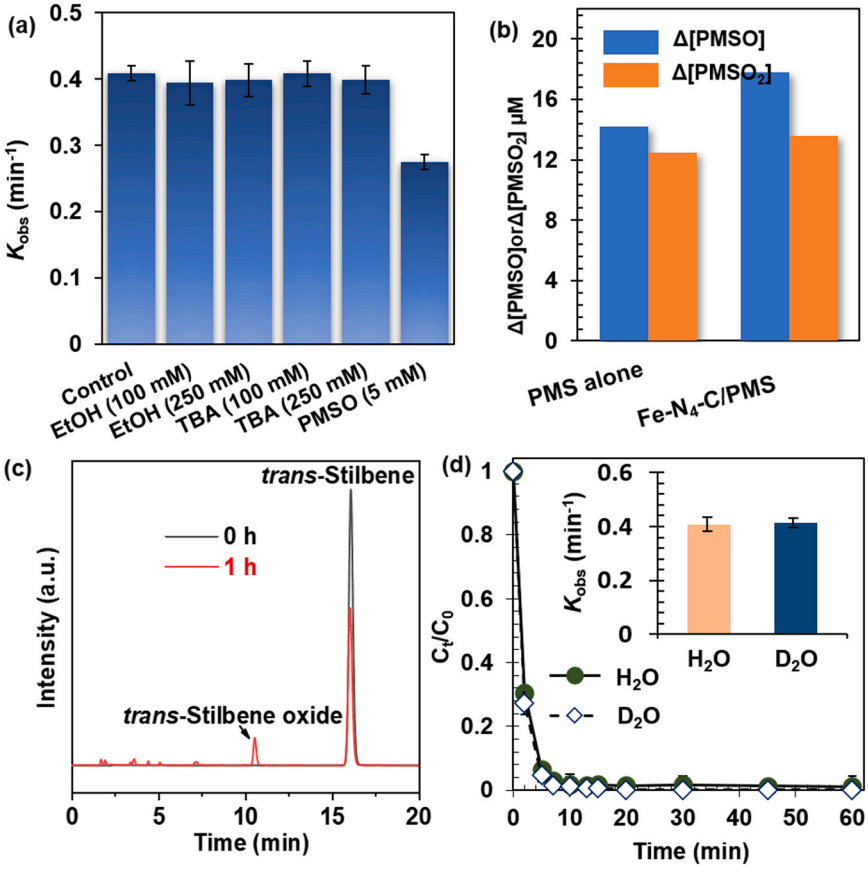

Fig. 4. (a) Quenching results in Fe-N_4-C/PMS systems; (b) PMSO consumption and $PMSO_2$ generation in PMS alone, and Fe-N_4-C/PMS systems; (c) The oxidation of trans-stilbene with Fe-N_4-C in the acetonitrile solution (80% acetonitrile; trans-stilbene: 1.0 mM; catalytic dosage: 0.1 g/L; PMS: 1.0 mM); (d) The k_{obs} values of NPX oxidation in H_2O and D_2O solutions. (The Fe-N_4-C was derived from 2.5 M of urea-saturated *Enteromorpha*; NPX: 10 mg/L; PMS: 1.0 mM; catalytic dosage: 0.1 g/L; pH: 6.0).

strong TEMP-$^1O_2$ signal in the Fe-N_4-C/PMS systems at 2 and 5 min (Fig. S24), and the signal was almost constant with the addition of NPX at 5 min. These results indicated that $^1O_2$ can be detected in the Fe-N_4-C/PMS system but contributes a negligible amount to NPX degradation. This was further confirmed by using the D_2O as a solvent, where replacing H_2O with a D_2O solvent only increased the k_{obs} value by about 2–10% (Fig. 4d). Basically, the roles of radicals accompanying with Fe(IV) and $^1O_2$ still showed negligible contributions towards NPX oxidation. As a result, NPX oxidation proceeding mainly through other pathways need to be well identified in the *Enteromorpha*-derived Fe-SACs/PMS system.

3.3. Mechanism of electron-transfer process (ETP) analysis

It was known that PMS can be activated by a variety of catalysts to form the surface activated complexes that directly oxidize organics via ETP [5,44]. The surface chemical evolution of catalysts with PMS can be studied by in situ Raman technique to investigate the ETP of *Enteromorpha*-derived Fe-SACs (Fe-N_4-C). As shown in Fig. 5a, when the Fe-N_4-C ccatalysts were added to the PMS solution, a new peak appeared at 836 cm^{-1} corresponding to activated peroxides (PMS*), because PMS bound to surface metal sites to form peroxide species (denoted Fe-N_4-C/PMS*). Compared with pure PMS solution, the characteristic vibration peak (HO-OSO_3^-) of O-O bond of PMS in both Fe-N_4-C/PMS systems (two Fe-N_4-C catalysts prepared by 2.5 M of urea and 5.0 M of urea saturation) shifts from 887 cm^{-1} to 890 cm^{-1}. In contrast, the Fe-N_2O_2 catalyst with low amounts of iron single sites only showed a small shift from 887 cm^{-1} to 888 cm^{-1}. This is due to the strong interaction between peroxide O-O bond and metal single-atom sites that changes the amplitude of tensile vibration. As a result, the metastable Fe-N_4-C/PMS* was formed by the strong binding of PMS with Fe-N_4-C, which was attached to the surface of the catalyst and subsequently oxidized NPX to generate SO_4^{2-}.

We further developed a galvanic oxidation system (GOS) to unveil the ETP between the metastable Fe-N_4-C/PMS* and NPX molecules since the electrons can transfer from the NPX molecules to Fe-N_4-C/PMS* complexes along with electron channel if the electron-transfer oxidation occurred in the catalytic systems [45]. The *Enteromorpha*-derived Fe-SACs (Fe-N_4-C, derived from 2.5 M of urea-saturated *Enteromorpha*) were immobilized onto the graphite electrode, and the NPX and PMS were added into two seperated cells connected via an agar salt bridge and an ampere meter (Fig. 5b). GOS coating with Fe-N_4-C in the background of PMS showed a high instantaneous current (64 μA). However, it was significantly decreased to 23 μA with the addition of phenanthroline in the Fe-N_4-C/PMS system (Fig. 5c). This result provides a solid evidence for supporting the high ETP triggerred by iron single-atom in *Enteromorpha*-derived Fe-SACs (Fe-N_4-C). We also observed the significantly decreased oxidation efficiency of NPX in Fe-N_4-C coated GOS with the presence of phenanthroline (Fig. 5d), unveiling that the strong ETP of Fe-N_4-C/PMS* complexes towards NPX degradation was primary originated from the iron centers rather than the metal-free counterparts.

The ETP in *Enteromorpha*-derived Fe-SACs/PMS systems for NPX oxidation was further confirmed via the open circuit potential tests. As shown in Fig. 5e, the open-circuit potential of glassy carbon electrode (GCE) coated with Fe-N_4-C (derived from 2.5 M of urea-saturated *Enteromorpha*) was significantly increased with the addition of PMS at 500 s. The results showed that the formation of Fe-N_4-C/PMS* complexes by PMS and catalyst could increase the potential of Fe-N_4-C. The open-circuit potential was significantly decreased after adding NPX at 3500 s, which was due to the redox reaction between NPX and Fe-N_4-C/PMS complex, resulting the the decomposition of surface complex. As a result, strong ETP occurs in Fe-N_4-C/PMS systems, with PMS as electron acceptor and NPX as electron donor. This phenomenon is also

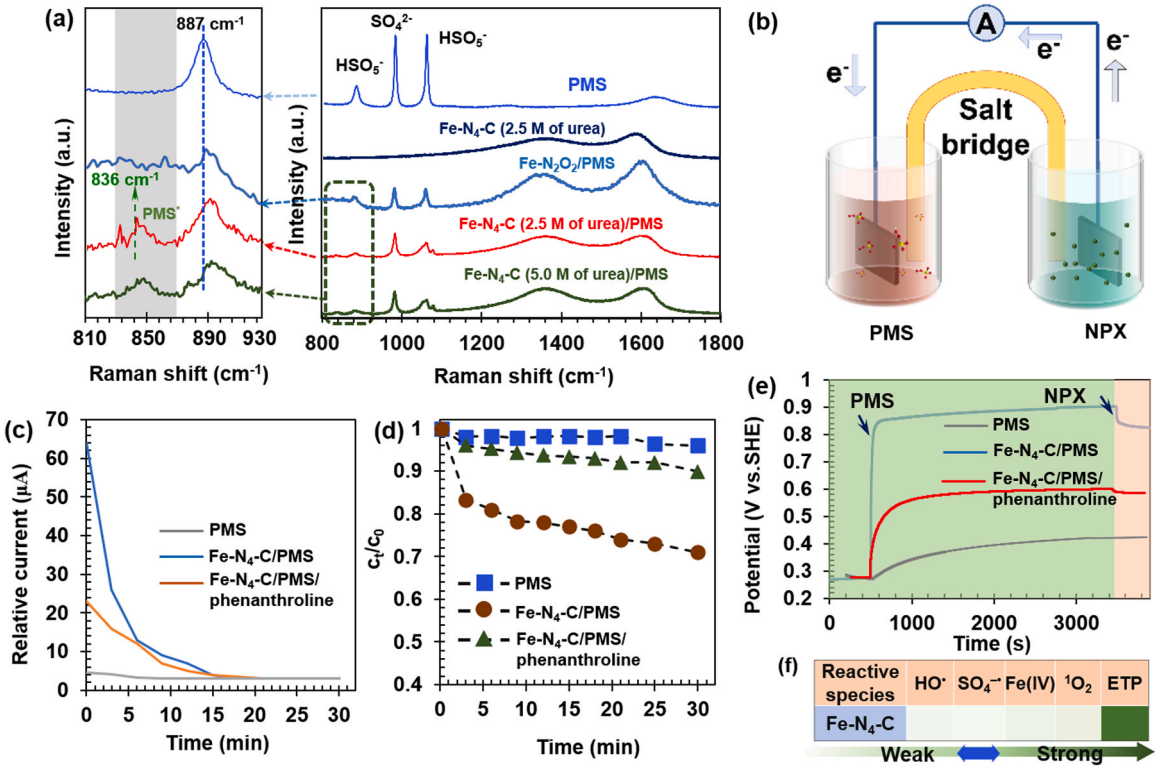

Fig. 5. (a) In situ Raman spectra of PMS, Fe-N_4-C, Fe-N_2O_2/PMS, and Fe-N_4-C/PMS; (b) The scheme of galvanic oxidation system (GOS); (c) Relative current of galvanic oxidation system GOS with the Fe-N_4-C/PMS, and Fe-N_4-C/PMS with the addition of iron screening agent, phenanthroline (The Fe-N_4-C was derived from 2.5 M of urea-saturated *Enteromorpha*); (d) Oxidation efficiency of NPX in Fe-N_4-C coated GOS with/without the presence of phenanthroline; (e) Open-circuit potential of Fe-N_4-C/PMS, and Fe-N_4-C/PMS with the addition of iron screening agent (phenanthroline); (f) The role of different species on the oxidation NPX.

complementary to the result of in situ Raman spectra. In addition, a significant decrease in the potential of Fe-N_4-C/PMS* complex was observed with the addition of iron screening agent (phenanthroline) in the Fe-N_4-C/PMS system; this indicated that the iron single atoms acted as the active sites for promoting the potential of Fe-N_4-C/PMS* complex. As a result, the role of different species on the oxidation NPX can be identified, which showed that ETP was the dominated pathway in Fe-N_4-C/PMS system (Fig. 5f).

3.4. Density functional theory (DFT) analysis

DFT calculations were further carried out to furnish theoretical analysis on the interaction of *Enteromorpha*-derived Fe-SACs (Fe-N_4-C) with PMS for NPX oxidation [1,46–49]. The images of two-dimensional electron density distribution (Fig. 6a and b) demonstrated the highest electron density of Fe atom in the Fe-N_4-C configuration as compared with that of N_4-C configuration, which can facilitate the attachment of PMS onto the iron single-atom sites in Fe-N_4-C. This was confirmed by the stronger adsorption energy (E_{ad}, −1.276 eV) of PMS onto Fe-N_4-C, which was significantly higher than that of N_4-C configuration (Fig. 6c and d). The high E_{ad} of PMS onto Fe-N_4-C therefore promoted the formation of Fe-N_4-C/PMS* complexes in the catalytic system. HOMO and LUMO analysis would help for the deeper understanding of the electron transfer between the NPX molecule and catalysts/PMS complexes [5]. Since LUMO is the Lowest Unoccupied Molecular Orbital, there are no electrons on LUMO and thus no electrons can be transferred from LUMO (−2.312 eV) of Fe-N_4-C/PMS to HOMO (−5.963 eV) of NPX. As a result, there was only one route for the electron transfer: HOMO of NPX to LUMO of Fe-N_4-C/PMS. LUMO of Fe-N_4-C/PMS and HOMO of various pollutants (e.g., NPX, BPA, SA, and CBZ) were given in Fig. 6e, and the HOMO-LUMO energy gaps are linearly correlated with the ln(k_{obs}) values of pollutants (Fig. 6f). This indicated that pollutants (e.g., NPX) with lower energy gaps could achieve a higher oxidation rate via a faster extraction of electrons from NPX by using the Fe-N_4-C as the conductive bridge. This process could facilitate the electron transfer from NPX to the activated PMS* , resulting in the fast NPX oxidation by ETP (Fig. 6g) [5].

3.5. NPX oxidation in Fe-N_4-C/CM system

The *Enteromorpha*-derived Fe-SACs (Fe-N_4-C, derived from 2.5 M of urea-saturated *Enteromorpha*) could be uniformly deposited on a commercial CM (10 cm × 25 cm, 2.0 mg Fe-N_4-C/cm^2 of CM) to form a Fe-N_4-C/CM system via a novel spraying-crosslinking method (Fig. 7a and b). Cross section morphology of the Fe-N_4-C/CM showed that the *Enteromorpha*-derived Fe-SACs were well deposited onto the surface of CM with average thickness of 20 μm (Fig. 7c). The hydrophilicity tests showed that both virgin CM and /CM required a very short time (0.36 s) for the drop entirely assimilation (Fig. 7d and e). Although the Fe-N_4-C catalysts formed a certain thickness structure on the surface of the CM, little effect on the hydrophilicity of the CM was observed; this may be due to the introduction of oxygen-containing groups during pickling and annealing in air, which formed more hydrogen bonds with water molecules and promoted water transport in the pores [50]. Of source, effect of introduced oxygen-containing groups on the catalytic performance should also be excluded.

Benefiting from its superior hydrophilicity, the Fe-N_4-C/CM only showed a very small decrease in water flux although the surface of coated CM was partially blocked by the catalysts (Fig. 8a). However, the water flux of Fe-N_4-C/CM can also keep constant for long-term operation. The continuous catalytic performance of Fe-N_4-C/CM for NPX degradation was tested using a flow through setup driven via a diaphragm pump (Fig. S25) [51–54]. The Fe-N_4-C/CM could achieve complete degradation of NPX via PMS activation under continuous Fenton-like system in different simulated and actual water matrixes, indicating the superiority of Fe-N_4-C/CM for organics oxidation via PMS activation (Fig. 8b). In contrast, virgin CM/PMS system exhibited very small NPX removal efficiency since the virgin CM was chemically inert towards PMS activation with ineffective membrane pore interception for low-weight organics. Considering that oxygen-containing groups might be introduced into CM materials during picking and annealing in air which might affected the catalytic performance, NPX oxidation performance of bare CM after picking and annealing was conducted which showed similar catalytic activity towards NPX as compared with the virgin CM (Fig. 8b). This result indicated that the oxygen-containing groups cannot affect the catalytic performance of Fe-N_4-C/CM for PMS activation. We also compared the Fe-N_4-C/CM system with other gravity

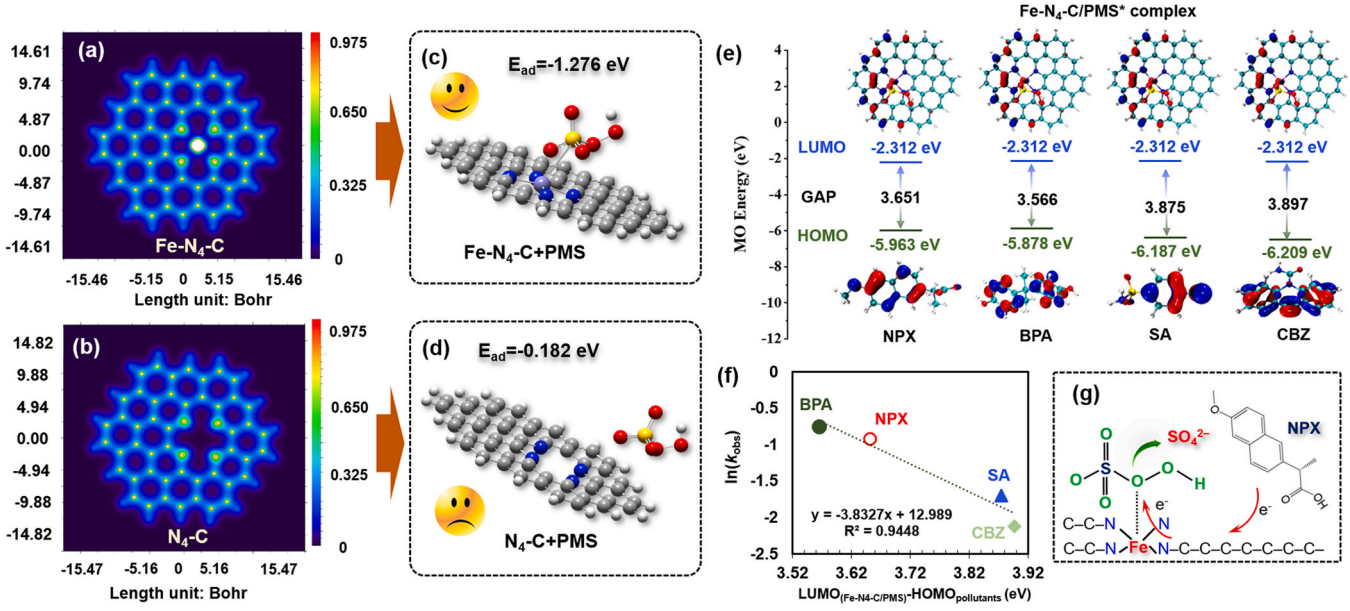

Fig. 6. Two-dimensional electron density distribution of (a) Fe-N_4-C configuration, and (b) N_4-C configuration; Adsorption energy of PMS onto (c) Fe-N_4-C configuration; and (d) N_4-C configuration; (e) Gap between HOMO of different pollutant molecules and LUMO of Fe-N_4-C/PMS* complex; (f) Linearity between $LUMO_{(Fe\text{-}N4\text{-}C/PMS)}$-$HOMO_{pollutants}$ and their ln(k_{obs}); (g) Scheme of ETP in Fe-N_4-C/PMS* system for NPX oxidation.

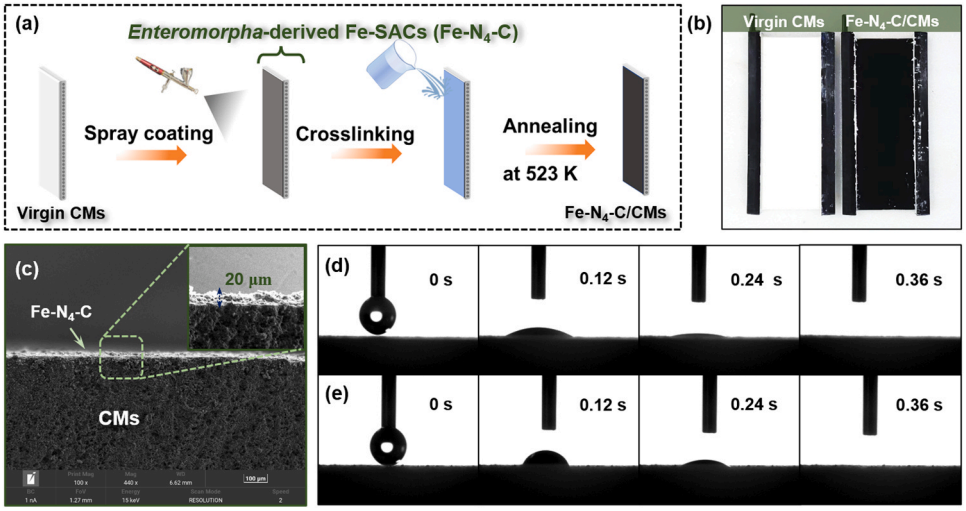

Fig. 7. (a) Fabricating scheme of *Enteromorpha*-derived Fe-SACs (Fe-N_4-C) deposited CM; (b) Real products of virgin CM and Fe-N_4-C/CM; (c) Cross section morphology of the Fe-N_4-C/CM; The contact angle of (d) virgin CM, and (e) Fe-N_4-C/CM.

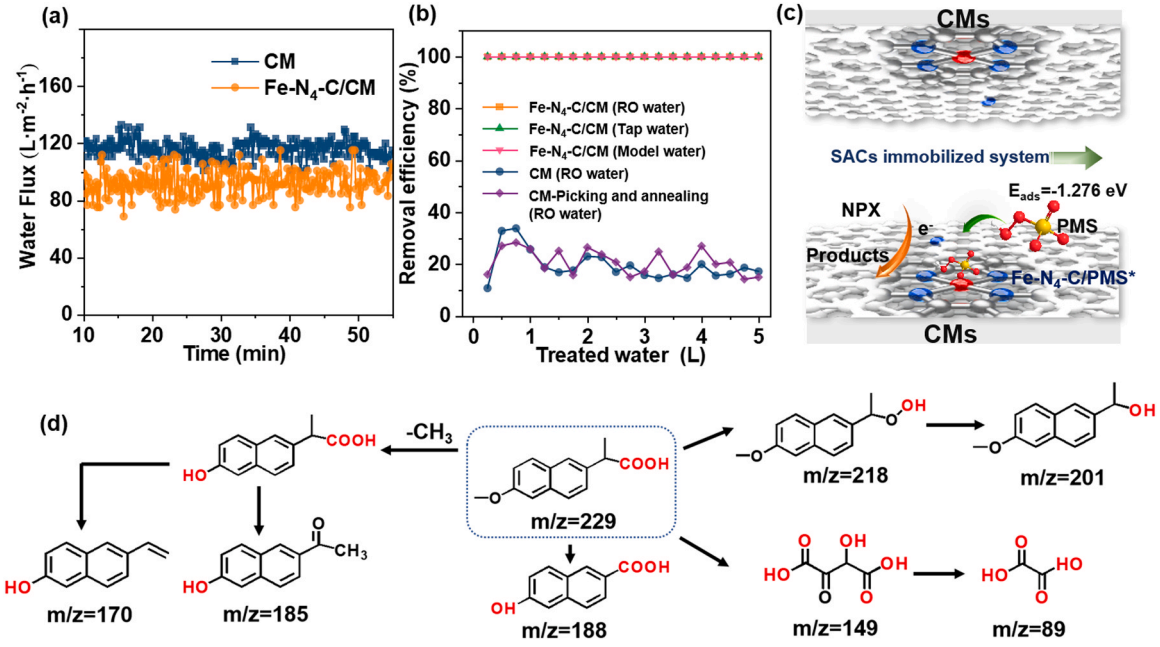

Fig. 8. (a) Water flux of virgin CM and Fe-N_4-C/CM (−0.03 MPa); (b) NPX removal in different membrane systems (The Fe-N_4-C was derived from 2.5 M of urea-saturated *Enteromorpha*; NPX: 250 μg/L, PMS: 1.0 mM); (c) Catalytic scheme of the Fe-N_4-C/CM for PMS activation; (d) Degradation products of NPX in the Fe-N_4-C/PMS system.

or pressure driven CM or organic membrane systems [50–55]. Results showed that the Fe-N_4-C/CM system could be more easily used in practical water oxidation due to its more stable catalytic activity with lower PMS dosage (Table S7). As a result, the immobilization of *Enteromorpha*-derived Fe-SACs (Fe-N_4-C) onto the CM with a ETP dominated pathway not only achieves modular integration of powder catalysts for actual wastewater treatment, but also help for the equipment development in Fenton-like system (Fig. 8c).

In addition, the degradation products of NPX in the Fe-N_4-C/PMS system was measured (Fig. S26, S27 and Fig. 8d). Since the low oxidation capacity as compared with that of radicals, some fractions of the NPX oxidation intermediates could be observed even after 20 min of degradation process. In addition, high amounts of SO_4^{2-} can be detected at 3, 7 and 20 min (Fig. S26 and S27). These SO_4^{2-} were derived from the metastable Fe-N_4-C/PMS* , which oxidized NPX and thereafter the PMS* was transformed to the SO_4^{2-}. As a result, the degradation products of NPX further provided an evidence of ETP in Fe-N_4-C/PMS system.

4. Conclusion

In this work, marine Fe-rich *Enteromorpha* was used as the iron precursor to prepare the atomically-dispersed Fe-SACs catalyst with iron content up to 1.55–1.60 wt%. The *Enteromorpha* is also a kind of pollution algae in the coastal areas of China. Therefore, this study has realized the resource utilization of *Enteromorpha* and provided a new idea for the preparation of SACs with more than 1 wt% Fe. The *Enteromorpha*-derived Fe-SACs showed well-dispersed single-atom structures with typical Fe–N_4-C coordination configuration, and no Fe clusters can be detected in the biomass-based carbon matrixes. The roles of radicals accompanying with Fe(IV) and $^1O_2$ showed minor contributions towards

NPX oxidation via PMS activation by the *Enteromorpha*-derived Fe-SACs. In contrast, We found that NPX oxidation was almost prominated by the ETP mechanism, and it was mostly triggered by Fe–N_4-C sites in *Enteromorpha*-derived Fe-SACs which was confirmed by the iron screening tests. We also prepared a CM coated with *Enteromorpha*-derived Fe-SACs for continuous Fenton-like system, which exhibited the stable water flux, promising mechanical stability and superior catalytic performance. Basically, this study provides an interesting fabrication strategy for SACs and also gives the new insights into catalytic pathways triggered by the Fe-SACs derived from Fe-rich biomass. The as-prepared *Enteromorpha*-derived Fe-SACs/CM could also exhibit promising performance in actual Fenton-like applications.

CRediT authorship contribution statement

Kexin Yin: Methodology, Formal analysis, Investigation, Writing – original draft, Visualization. **Lijing Peng:** Visualization. **DongDong Chen:** Formal analysis, Investigation. **Siyi Liu:** Methodology. **Yujie Zhang:** Methodology. **Baoyu Gao**: Methodology. **Kaifang Fu:** Visualization. **Yanan Shang:** XASF analysis, DFT calculation. **Xing Xu:** Resources, Writing – review & editing, Supervision.

Declaration of Competing Interest

The authors declare that they have no known competing financial interests or personal relationships that could have appeared to influence the work reported in this paper.

Data availability

Data will be made available on request.

Acknowledgments

The work was supported by National Natural Science Foundation of China (52170086), Shandong Provincial Excellent Youth (ZR2022YQ47) and Natural Science Foundation of Shandong Province (ZR2021ME013). The authors also want to thank Conghua Qi from Shiyanjia Lab (www.shiyanjia.com) for DFT calculations.

Appendix A. Supporting information

Supplementary data associated with this article can be found in the online version at doi:10.1016/j.apcatb.2023.122951.

References

[1] Y. Bao, C. Lian, K. Huang, H. Yu, W. Liu, J. Zhang, M. Xing, Generating high-valent iron-oxo identical with $\equiv Fe^{IV}=O$ complexes in neutral microenvironments through peroxymonosulfate activation by Zn-Fe layered double hydroxides, Angew. Chem. Int. Ed., 61 (2022) e202209542. https://doi.org/10.1002/ange.202209542.

[2] W. Liu, P. Fu, Y. Zhang, H. Xu, H. Wang, M. Xing, Efficient hydrogen production from wastewater remediation by piezoelectricity coupling advanced oxidation processes, Proc. Natl. Acad. Sci. 120 (2023), e2218813120, https://doi.org/10.1073/pnas.2218813120.

[3] X. Liu, X. Yan, W. Liu, Q. Yan, M. Xing, Switching of radical and nonradical pathways through the surface defects of Fe_3O_4/MoO_xS_y in a Fenton-like reaction, Sci. Bull. 68 (2023) 603–612, https://doi.org/10.1016/j.scib.2023.02.031.

[4] Y. Shang, X. Liu, Y. Li, Y. Gao, B. Gao, X. Xu, Q. Yue, Boosting Fenton-like reaction by reconstructed single Fe atom catalyst for oxidizing organics: Synergistic effect of conjugated π-π sp^2 structured carbon and isolated Fe-N_4 sites, Chem. Eng. J. 446 (2022), 137120, https://doi.org/10.1016/j.cej.2022.137120.

[5] M. Yang, Z. Hou, X. Zhang, B. Gao, Y. Li, Y. Shang, Q. Yue, X. Duan, X. Xu, Unveiling the origins of selective oxidation in single-atom catalysis via Co–N_4–C intensified radical and nonradical pathways, Environ. Sci. Technol. 56 (2022) 11635–11645, https://doi.org/10.1021/acs.est.2c01261.

[6] Z.Y. Guo, Y. Si, W.Q. Xia, F. Wang, H.Q. Liu, C. Yang, W.J. Zhang, W.W. Li, Electron delocalization triggers nonradical Fenton-like catalysis over spinel oxides, Proc. Natl. Acad. Sci. 119 (2022), e2201607119, https://doi.org/10.1073/pnas.2201607119.

[7] L.S. Zhang, X.H. Jiang, Z.A. Zhong, L. Tian, Q. Sun, Y.T. Cui, X. Lu, J.P. Zou, S. L. Luo, Carbon nitride supported high-loading Fe single-atom catalyst for activation of peroxymonosulfate to generate $^1O_2$ with 100% selectivity, Angew. Chem. Int. Ed. 60 (2021) 21751–21755, https://doi.org/10.1002/anie.202109488.

[8] J. Yang, D. Zeng, Q. Zhang, R. Cui, M. Hassan, L. Dong, J. Li, Y. He, Single Mn atom anchored on N-doped porous carbon as highly efficient Fenton-like catalyst for the degradation of organic contaminants, Appl. Catal. B: Environ. 279 (2020), 119363, https://doi.org/10.1016/j.apcatb.2020.119363.

[9] W. Du, Q. Zhang, Y. Shang, W. Wang, Q. Li, Q. Yue, B. Gao, X. Xu, Sulfate saturated biosorbent-derived Co-S@NC nanoarchitecture as an efficient catalyst for peroxymonosulfate activation, Appl. Catal. B: Environ. 262 (2020), 118302, https://doi.org/10.1016/j.apcatb.2019.118302.

[10] C. Jiang, S. Garg, T.D. Waite, Hydroquinone-mediated redox cycling of iron and concomitant oxidation of hydroquinone in oxic waters under acidic conditions: comparison with iron–natural organic matter interactions, Environ. Sci. Technol. 49 (2015) 14076–14084, https://doi.org/10.1021/acs.est.5b03189.

[11] Y.Y. Ahn, H. Bae, H.I. Kim, S.H. Kim, J.H. Kim, S.G. Lee, J. Lee, Surface-loaded metal nanoparticles for peroxymonosulfate activation: efficiency and mechanism reconnaissance, Appl. Catal. B: Environ. 241 (2019) 561–569, https://doi.org/10.1016/j.apcatb.2018.09.056.

[12] X. Li, X. Huang, S. Xi, S. Miao, J. Ding, W. Cai, S. Liu, X. Yang, H. Yang, J. Gao, J. Wang, Y. Huang, T. Zhang, B. Liu, Single cobalt atoms anchored on porous N-doped graphene with dual reaction sites for efficient Fenton-like catalysis, J. Am. Chem. Soc. 140 (2018) 12469–12475, https://doi.org/10.1021/jacs.8b05992.

[13] S. Wang, J. Tian, L. Jia, J. Jia, S. Shan, Q. Wang, F. Cui, Removal of aqueous organic contaminants using submerged ceramic hollow fiber membrane coupled with peroxymonosulfate oxidation: Comparison of CuO catalyst dispersed in the feed water and immobilized on the membrane, J. Membr. Sci. 618 (2021), 118707, https://doi.org/10.1016/j.memsci.2020.118707.

[14] Z. Yang, J. Qian, A. Yu, B. Pan, Singlet oxygen mediated iron-based Fenton-like catalysis under nanoconfinement, PNAS 116 (2019) 6659–6664, https://doi.org/10.1073/pnas.1819382116.

[15] Y. Zong, Y. Shao, Y. Zeng, B. Shao, L. Xu, Z. Zhao, W. Liu, D. Wu, Enhanced oxidation of organic contaminants by iron(II)-activated periodate: the significance of high-valent iron–oxo species, Environ. Sci. Technol. 55 (2021) 7634–7642, https://doi.org/10.1021/acs.est.1c00375.

[16] W.J. Wang, H.N. Wang, G.Y. Li, T.C. An, H.J. Zhao, P.K. Wong, Catalyst-free activation of persulfate by visible light for water disinfection: Efficiency and mechanisms, Water Res. 157 (2019) 106–118, https://doi.org/10.1016/j.watres.2019.03.071.

[17] W.J. Wang, H.N. Wang, G.Y. Li, P.K. Wong, T.C. An, Visible light activation of persulfate by magnetic hydrochar for bacterial inactivation: efficiency, recyclability and mechanisms, Water Res. 176 (2020), 115746, https://doi.org/10.1016/j.watres.2020.115746.

[18] J. Miao, Y. Zhu, J. Lang, J. Zhang, S. Cheng, B. Zhou, L. Zhang, P.J.J. Alvarez, M. Long, Spin-state-dependent peroxymonosulfate activation of single-atom M–N moieties via a radical-free pathway, ACS Catal. 11 (2021) 9569–9577, https://doi.org/10.1021/acscatal.1c02031.

[19] Y. Shang, X. Xu, B. Gao, S. Wang, X. Duan, Single-atom catalysis in advanced oxidation processes for environmental remediation, Chem. Soc. Rev. 50 (2021) 5281–5322, https://doi.org/10.1039/D0CS01032D.

[20] H. Fei, J. Dong, D. Chen, T. Hu, X. Duan, I. Shakir, Y. Huang, X. Duan, Single atom electrocatalysts supported on graphene or graphene-like carbons, Chem. Soc. Rev. 48 (2019) 5207–5241, https://doi.org/10.1039/C9CS00422J.

[21] Z.X. Wei, Y.T. Zhu, J.Y. Liu, Z.C. Zhang, W.P. Hu, H. Xu, Y.Z. Feng, J.M. Ma, Recent advance in single-atom catalysis, Rare Met. 40 (2021) 767–789, https://doi.org/10.1007/s12598-020-01592-1.

[22] X. Xie, L. Shang, X. Xiong, R. Shi, T. Zhang, Fe single-atom catalysts on MOF-5 derived carbon for efficient oxygen reduction reaction in proton exchange membrane fuel cells, Adv. Energy Mater. 12 (2022), 2102688, https://doi.org/10.1002/aenm.202102688.

[23] Q. Wang, L. Shang, D. Sun-Waterhouse, T. Zhang, G. Waterhouse, Engineering local coordination environments and site densities for high-performance Fe-N-C oxygen reduction reaction electrocatalysis, SmartMat 2 (2021) 154–175, https://doi.org/10.1002/smm2.1033.

[24] X. Yan, Y. Jia, K. Wang, Z. Jin, C.L. Dong, Y.C. Huang, J. Chen, X. Yao, Controllable synthesis of Fe–N_4 species for acidic oxygen reduction, Carbon Energy 2 (2020) 452–460, https://doi.org/10.1002/cey2.47.

[25] M.H. Li, H.F. Wang, W. Luo, P.C. Sherrell, J. Chen, J.P. Yang, Heterogeneous single-atom catalysts for electrochemical CO_2 reduction reaction, Adv. Mater. 32 (2020), 2001848, https://doi.org/10.1002/adma.202001848.

[26] Q.Q. Zhang, J.Q. Guan, Single-atom catalysts for electrocatalytic applications, Adv. Funct. Mater. 30 (2020), 2000768, https://doi.org/10.1002/adfm.202000768.

[27] F. Franco, C. Rettenmaier, H.S. Jeon, B. Roldan Cuenya, Transition metal-based catalysts for the electrochemical CO_2 reduction: from atoms and molecules to nanostructured materials, Chem. Soc. Rev. 49 (2020) 6884–6946, https://doi.org/10.1039/D0CS00835D.

[28] M. Cheng, C. Lai, Y. Liu, G. Zeng, D. Huang, C. Zhang, L. Qin, L. Hu, C. Zhou, W. Xiong (Eds.), Met.-Org. Framew. highly Effic. Heterog. Fenton- Catal., Coord. Chem. Rev. 368 (2018) 80–92, https://doi.org/10.1016/j.ccr.2018.04.012.

[29] P. Cui, C. Liu, X. Su, Q. Yang, L. Ge, M. Huang, F. Dang, T. Wu, Y. Wang, Atomically dispersed manganese on biochar derived from a hyperaccumulator for photocatalysis in organic pollution remediation, Environ. Sci. Technol. 56 (2022) 8034–8042, https://doi.org/10.1021/acs.est.2c00992.

[30] Y. Shang, X. Duan, S. Wang, Q. Yue, B. Gao, X. Xu, Carbon-based single atom catalyst: Synthesis, characterization, DFT calculations, Chin. Chem. Let. 33 (2022) 663–673, https://doi.org/10.1016/j.cclet.2021.07.050.
[31] Y. Lei, F. Yang, H. Xie, Y. Lei, X. Liu, Y. Si, H. Wang, Biomass in situ conversion to Fe single atomic sites coupled with Fe_2O_3 clusters embedded in porous carbons for the oxygen reduction reaction, J. Mater. Chem. A 8 (2020) 20629–20636, https://doi.org/10.1039/D0TA06022D.
[32] X. Wang, J. Du, Q. Zhang, L. Gu, L. Cao, H.-P. Liang, In situ synthesis of sustainable highly efficient single iron atoms anchored on nitrogen doped carbon derived from renewable biomass, Carbon 157 (2020) 614–621, https://doi.org/10.1016/j.carbon.2019.10.054.
[33] Z. Li, K. Li, S. Ma, B. Dang, Y. Li, H. Fu, J. Du, Q. Meng, Activation of peroxymonosulfate by iron-biochar composites: Comparison of nanoscale Fe with single-atom Fe, J. Colloid Inter. Sci. 582 (2021) 598–609, https://doi.org/10.1016/j.jcis.2020.08.049.
[34] L. Peng, X. Duan, Y. Shang, B. Gao, X. Xu, Engineered carbon supported single iron atom sites and iron clusters from Fe-rich Enteromorpha for Fenton-like reactions via nonradical pathways, Appl. Catal. B: Environ. 287 (2021), 119963, https://doi.org/10.1016/j.apcatb.2021.119963.
[35] C. Zhu, Y. Nie, F. Cun, Y. Wang, Z. Tian, F. Liu, Two-step pyrolysis to anchor ultrahigh-density single-atom FeN_5 sites on carbon nitride for efficient Fenton-like catalysis near 0 °C, Appl. Catal. B: Environ. 319 (2022), 121900, https://doi.org/10.1016/j.apcatb.2022.121900.
[36] D. Zhang, K. Yin, Y.H. Tang, Y.F. Wei, H.F. Tang, Yi Du, H.L. Liu, Y.Q. Chen, C. B. Liu, Hollow sea-urchin-shaped carbon-anchored single-atom iron as dual-functional electro-Fenton catalysts for degrading refractory thiamphenicol with fast reaction kinetics in a wide pH range, Chem. Eng. J. 427 (2022), 130996, https://doi.org/10.1016/j.cej.2021.130996.
[37] T. Lu, Q.X. Chen, Interaction Region Indicator: A simple real space function clearly revealing both chemical bonds and weak interactions, Chem. Methods 1 (2021) 231–389, https://doi.org/10.1002/cmtd.202100007.
[38] F. Wang, Y. Wang, Y. Feng, Y. Zeng, Z. Xie, Q. Zhang, Y. Su, P. Chen, Y. Liu, K. Yao, W. Lv, G. Liu, Novel ternary photocatalyst of single atom-dispersed silver and carbon quantum dots co-loaded with ultrathin g-C_3N_4 for broad spectrum photocatalytic degradation of naproxen, Appl. Catal. B: Environ. 221 (2018) 510–520, https://doi.org/10.1016/j.apcatb.2017.09.055.
[39] Y. Qi, J. Li, Y. Zhang, Q. Cao, Y. Si, Z. Wu, M. Akram, X. Xu, Novel lignin-based single atom catalysts as peroxymonosulfate activator for pollutants degradation: Role of single cobalt and electron transfer pathway, Appl. Catal. B: Environ. 286 (2021), 119910, https://doi.org/10.1016/j.apcatb.2021.119910.
[40] Z. Liu, X. Sun, Z. Sun, CoNi alloy anchored onto N-doped porous carbon for the removal of sulfamethoxazole: Catalyst, mechanism, toxicity analysis, and application, Chemosphere 308 (2022), 136291, https://doi.org/10.1016/j.chemosphere.2022.136291.
[41] H. Chi, X. He, J. Zhang, D. Wang, X. Zhai, J. Ma, Hydroxylamine enhanced degradation of naproxen in Cu^{2+} activated peroxymonosulfate system at acidic condition: Efficiency, mechanisms and pathway, Chem. Eng. J. 361 (2019) 764–772, https://doi.org/10.1016/j.cej.2018.12.114.
[42] G.V. Buxton, C.L. Greenstock, W.P. Helman, A.B. Ross, Critical review of rate constants for reactions of hydrated electrons, hydrogen atoms and hydroxyl radicals (·OH/·O^-) in aqueous solution, J. Phy. Chem. Refer. Data 17 (1988) 513–886.
[43] P. Neta, J. Grodkowski, A.B. Ross, Rate constants for reactions of aliphatic carbon-centered radicals in aqueous solution, J. Phy. Chem. Refer. Data 25 (1996) 709–1050.
[44] E.T. Yun, J.H. Lee, J. Kim, H.D. Park, J. Lee, Identifying the nonradical mechanism in the peroxymonosulfate activation process: singlet oxygenation versus mediated electron transfer, Environ. Sci. Technol. 52 (2018) 7032–7042, https://doi.org/10.1021/acs.est.8b00959.
[45] M. Luo, H. Zhang, P. Zhou, Z. Xiong, B. Huang, J. Peng, R. Liu, W. Liu, B. Lai, Efficient activation of ferrate(VI) by colloid manganese dioxide: Comprehensive elucidation of the surface-promoted mechanism, Water Res. 215 (2022), 118243, https://doi.org/10.1016/j.watres.2022.118243.
[46] F. Chen, X.L. Wu, C.Y. Shi, H.J. Lin, J.R. Chen, Y.P. Shi, S.B. Wang, X.G. Duan, Molecular engineering toward pyrrolic N-rich M-N-4 (M = Cr, Mn, Fe, Co, Cu) single-atom sites for enhanced heterogeneous Fenton-like reaction, Adv. Funct. Mater. 31 (2021), https://doi.org/10.1002/adfm.202007877.
[47] Q.Y. Wu, J. Wang, Z.W. Wang, Y.L. Xu, Z.H. Xing, X.Y. Zhang, Y.T. Guan, G.F. Liao, X.Z. Li, High-loaded single Cu atoms decorated on N-doped graphene for boosting Fenton-like catalysis under neutral pH, J. Mater. Chem. A 8 (2020) 13685–13693, https://doi.org/10.1039/D0TA04943C.
[48] Y. Gao, X.G. Duan, B. Li, Q.Q. Jia, Y. Li, X.B. Fan, F.B. Zhang, G.L. Zhang, S. B. Wang, W.C. Peng, Fe containing template derived atomic Fe-N-C to boost Fenton-like reaction and charge migration analysis on highly active Fe-N-4 sites, J. Mater. Chem. A 9 (2021) 14793–14805, https://doi.org/10.1039/D1TA02446A.
[49] F. Chen, L.L. Liu, J.H. Wu, X.H. Rui, J.J. Chen, Y. Yu, Single-atom iron anchored tubular g-C_3N_4 catalysts for ultrafast Fenton-like reaction: roles of high-valency iron-oxo species and organic radicals, Adv. Mater. 34 (2022), 2202891, https://doi.org/10.1002/adma.202202891.
[50] P. Duan, X. Xu, K. Guo, Q. Yue, B. Gao, Peroxymonosulfate activation on a chainmail catalyst via an electron shuttle mechanism for efficient organic pollutant removal, Appl. Catal. B: Environ. 316 (2022), 121695, https://doi.org/10.1016/j.apcatb.2022.121695.
[51] X. Wu, K. Rigby, D. Huang, T. Hedtke, X. Wang, M.W. Chung, S. Weon, E. Stavitski, J.H. Kim, Single-atom cobalt incorporated in a 2D graphene oxide membrane for catalytic pollutant degradation, Environ. Sci. Technol. 56 (2022) 1341–1351, https://doi.org/10.1021/acs.est.1c06371.
[52] Y. Bao, W.J. Lee, T.T. Lim, R. Wang, X. Hu, Pore-functionalized ceramic membrane with isotropically impregnated cobalt oxide for sulfamethoxazole degradation and membrane fouling elimination: synergistic effect between catalytic oxidation and membrane separation, Appl. Catal. B: Environ. 254 (2019) 37–46, https://doi.org/10.1016/j.apcatb.2019.04.081.
[53] H. Wu, X. Xu, L. Shi, Y. Yin, L.C. Zhang, Z. Wu, X. Duan, S. Wang, H. Sun, Manganese oxide integrated catalytic ceramic membrane for degradation of organic pollutants using sulfate radicals, Water Res. 167 (2019), 115110, https://doi.org/10.1016/j.watres.2019.115110.
[54] Y. Liu, Q. Lin, Y. Guo, J. Zhao, X. Luo, H. Zhang, G. Li, H. Liang, The nitrogen-doped multi-walled carbon nanotubes modified membrane activated peroxymonosulfate for enhanced degradation of organics and membrane fouling mitigation in natural waters treatment, Water Res. 209 (2021), 117960, https://doi.org/10.1016/j.watres.2021.117960.
[55] C. Chu, J. Yang, X. Zhou, D. Huang, H. Qi, S. Weon, J. Li, M. Elimelech, A. Wang, J. H. Kim, Cobalt single atoms on tetrapyridomacrocyclic support for efficient peroxymonosulfate activation, Environ. Sci. Technol. 55 (2020) 1242–1250, https://doi.org/10.1021/acs.est.0c06086.